Separation Studies on Sphere and Cube Clusters in Mach 12 Flow

Dániel G. Kovács[1], Guillaume Grossir[2], Grigorios Dimitriadis[3], Olivier Chazot[4]

Abstract

The present study investigates the aerodynamic separation of compact fragment clusters composed of spheres and cubes. This experimental analysis was conducted in the VKI Longshot hypersonic wind tunnel at Mach 12 flow conditions, using a dual camera free-flight testing methodology. The test articles are initially confined in a sabot, which separates into two pieces and exposes the models to the freestream upon the arrival of the flow. Experiments on clusters of 11 spheres yielded a reasonable agreement regarding the mean terminal velocities with data available in the literature. Increasing the sphere population to 36, yielded greater object spread. Tests on clusters of 11 cubes, which produce a lateral force at most attitudes even individually, demonstrated significantly larger object dispersal, higher lateral terminal velocities, and larger maxima. To draw clear conclusions and to define adequately the separation dynamics on a macroscopic scale, a high number of repeat tests are required, and the problem must be assessed on a statistical basis.

Keywords: *hypersonic, free-flight testing, separation dynamics, cluster break-up, space debris*

Nomenclature

Latin

D	–	diameter
R	–	radius
t	–	time
Re	–	Reynolds number
V	–	velocity

Greek

ρ	–	density

τ	–	time scale

Subscripts

c	–	cluster
m	–	meteor/model
s	–	scale
T	–	terminal
$unit$	–	relative to 1m
∞	–	freestream quantity

1. Introduction

During atmospheric entry, the aerodynamic separation of disintegrating spacecraft components or meteor pieces highly influences the force and thermal loads the fragments are exposed to and, therefore, also their demisability and the ground footprint. Due to the complexity of this phenomenon, Design for Demise tools often neglect or oversimplify the dispersion of the fragments and the interactions between the components, considering them as independent trajectories as soon as a

---

[1] *von Karman Institute for Fluid Dynamics / University of Liège, Waterloosesteenweg 72, B-1640, Sint-Genesius-Rode, Belgium / Allée de la Découverte 9, B-4000, Liège, Belgium,* daniel.gabor.kovacs@vki.ac.be

[2] *von Karman Institute for Fluid Dynamics, Waterloosesteenweg 72, B-1640, Sint-Genesius-Rode, Belgium,* guillaume.grossir@vki.ac.be

[3] *University of Liège / von Karman Institute for Fluid Dynamics, Allée de la Découverte 9, B-4000, Liège, Belgium / Waterloosesteenweg 72, B-1640, Sint-Genesius-Rode, Belgium,* gdimitriadis@uliege.be

[4] *von Karman Institute for Fluid Dynamics, Waterloosesteenweg 72, B-1640, Sint-Genesius-Rode, Belgium,* olivier.chazot@vki.ac.be

structural limit triggers the fragmentation event. Studying the behavior of proximal bodies and clusters is required to develop improved separation models that can improve demisability predictions.

Separation studies were first conducted by [1], [2], who described the dynamics of the meteorite fragmentation process with an equation for the expected lateral terminal velocity:

$$V_T = \sqrt{\frac{3}{2} \cdot C \cdot \frac{R_1}{R_2} \cdot \frac{\rho_\infty}{\rho_m}} \cdot V \qquad (1)$$

where C is a separation constant, R_1 and R_2 are the primary and secondary object's radii, ρ_∞ is the freestream density, and ρ_m and V are the density and speed of the meteorite. Extensive investigations of the interaction of two spheres by [3], [4], [5], [6], various studies on two bodies of distinct shapes [7], [8], [9], and some works on sphere clusters [10], [11], proved that the interactions between disintegrated spacecraft components or meteor fragments can increase the lateral velocities of the pieces, which enhances the object spreading. When moving from spherical geometries towards objects that can create lift at certain attitudes, the separation speed can increase even further [7], [9], and the behavior becomes case-dependent and very sensitive to the objects' initial orientation. The studies of [10], [11] have shown that increasing the number of objects in the cluster yields elevated separation velocities.

The current research aims to study the dispersion of sphere and cube clusters in a higher Mach number regime, where primary fragmentation events are typically expected during atmospheric entry. Clusters of 11 spheres, 11 cubes, and 36 spheres were tested. This study allows comparisons of lateral terminal velocities between the current Mach 12 and the previous Mach 6 sphere cluster experiments conducted by [11]. Furthermore, the effect of the objects' geometry and the influence of the cluster size is analyzed. The manuscript's structure is as follows: Section 2 introduces the experimental tools. This section explains the VKI Longshot facility, the freestream flow conditions, the free-flight testing apparatus, and the campaign's test matrix, with a detailed description of the model sizing and material selection. Section 3 elaborates on the image and trajectory processing methodology. Section 4 summarizes the experimental results, and Section 5 discusses the outcomes of the research.

2. Experimental Tools

2.1. The VKI Longshot Facility

The main facility at the von Karman Institute (VKI) for hypersonic free-flight testing of space debris objects is the VKI Longshot, illustrated in Fig 1. The facility operates based on the principle of a gun tunnel and can reproduce the high Mach and Reynolds numbers encountered during atmospheric entry. The current test campaign is with the Mach 12 contoured nozzle and Nitrogen test gas.
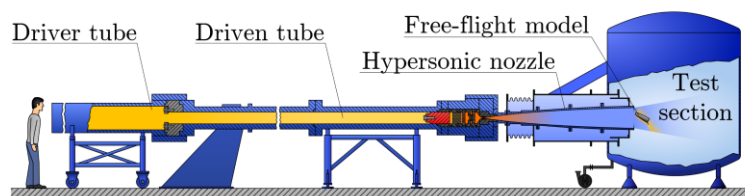

Fig 1. The VKI Longshot wind tunnel. [12]

A well-characterized operational point is selected, determined by the combination of the driver tube pressure, driven tube pressure, and the piston mass, providing unit Reynolds numbers decaying from Re_{unit} = 5.4· 10^6 1/m to 3.9·10^6 1/m. The 426 mm exit diameter nozzle provides a core flow of ~220 mm [13] in a useful test window of approximately 20 ms.

2.2. Flow conditions

The characterization of the flow conditions during Longshot experiments relies on the simultaneous measurement of the Pitot pressure, the freestream static pressure and the stagnation point heat-flux. Placing probes in the freestream permits the accurate computation of the wind properties; however, they occupy a significant section of the test volume and, therefore, might perturb the flow upstream of the free-flying objects. In order to avoid such flow disturbances, the probe set was omitted with the aim of relying on the repeatability of the flow conditions. The Pitot probe was employed exclusively in

a few experiments to verify the reproduction of the freestream properties via a comparison between the Pitot traces and the reservoir pressure signals (measured with a pressure tap upstream of the nozzle). Fig 2 presents the variation of the reservoir pressure and the Pitot pressure compared to a reference signal corresponding to the same operating conditions. Both pressure quantities are in agreement with the reference data. Since the Pitot probe was placed close to the edge of the core flow region and approximately 170 mm downstream, the shedding sabot pieces and the cluster fragments caused perturbations in its initial signal. A coalescence is visible during the 3.5-16 ms time frame, after which the core flow closes onto the probe. The plot on the right-hand side shows curve-fitted freestream quantities derived from the reference dataset, which were used afterward throughout the evaluation of the cluster experiments.
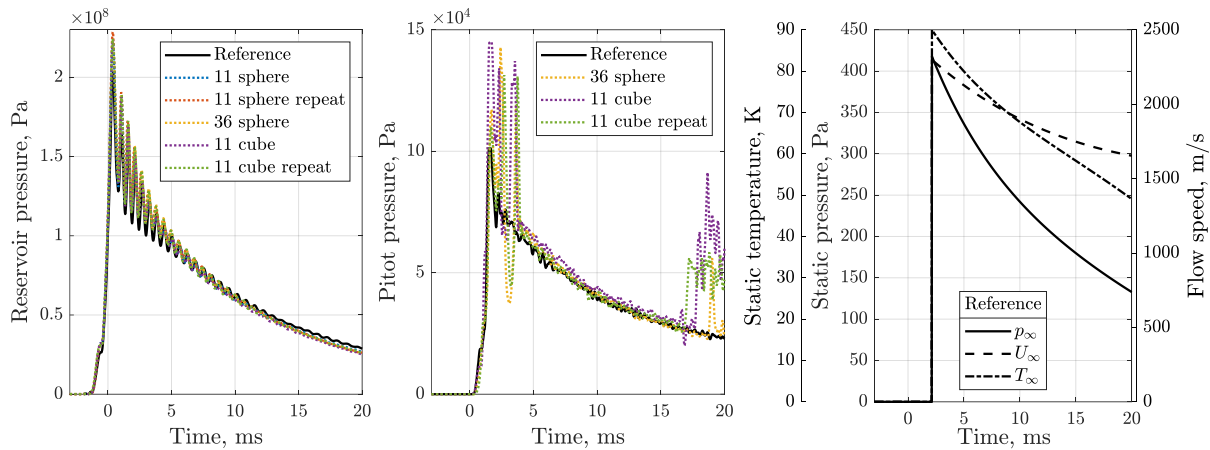

Fig 2. Comparison of a reference reservoir and Pitot pressure trace with the signals recorded during the current campaign. Freestream flow properties derived from the reference dataset.

2.3. Free-flight testing in the VKI Longshot

In free-flight experiments, the test articles are initially mounted using expendable supports that release the model upon the arrival of the flow, thereafter allowing unconstrained flight. Knowing the flow conditions, the inertial properties of the test model, and the local gravitational acceleration enables the computation of the aerodynamic load coefficients. Optical tracking methods require the double differentiation of the trajectory signal; however, they have moderate spatial (only visibility-related) constraints and may allow the tracking of the actual position even if the test models present moderate overlaps. The object tracking methodology relies on a silhouette-based position detection method; hence, the contour of the objects is of interest. The free-flight test setup of the VKI Longshot is presented in Fig 3 with a top and a side view sketch.
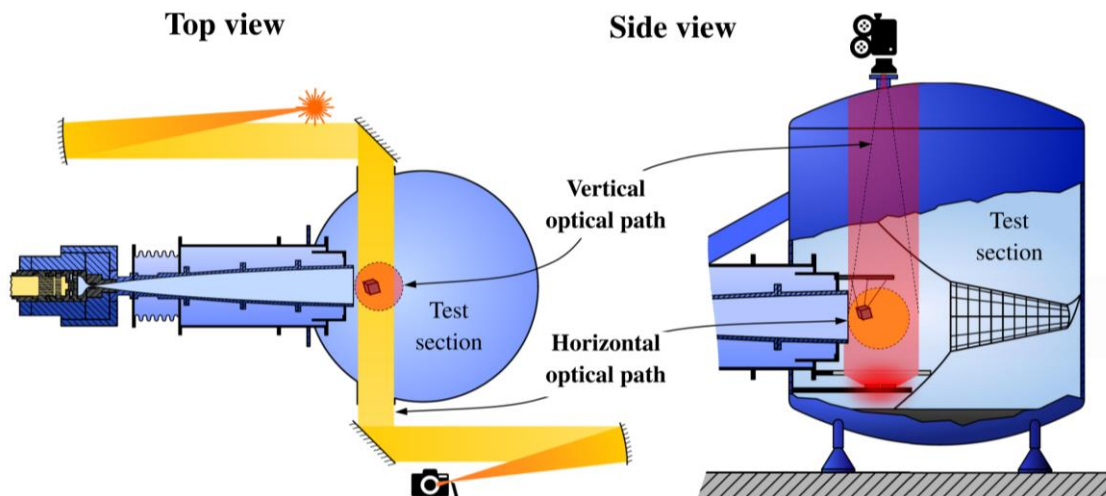

Fig 3. The dual camera optical setup employs a schlieren side view and a backlit top view. [14]

The equipment comprises two cameras (and their individual illumination setup) that record the experiments from two closely orthogonal perspectives. Both optical systems are independent of the wind tunnel to mitigate vibrations/excitations originating from the facility's operation. The wind tunnel's horizontal Z-type schlieren system provides an orthographically projected side view. The second optical path is vertical; a downward-looking camera is mounted above the test section, recording a backlit perspective-projected top view. The placement of the cameras and the backlighting setup are illustrated with photos in Fig 4.

The side view is recorded by a SpeedSense M310 high-speed camera equipped with a 200 mm objective, and a Phantom v2012 high-speed camera captures the top view with a variable zoom objective fixed at 200 mm. Due to the different capabilities of the cameras, the two videos were recorded at different resolutions and frame rates. The side perspective has a frame rate of 5 kHz with 6.52 µs exposure time and a resolution of 896x720 pixels, while the top is captured at a 20 kHz sampling rate with 4.98 µs exposure on a 1280x800 pixel resolution. Both cameras are triggered with a TTL signal supplied by a Stanford Research Systems DG535 Pulse generator based on the recoil of the driven tube. Due to the different sampling rates, frame locking between the cameras is not possible without an external synchronizer. The frame delay between the side and the top view changes from test to test and is considered during the processing.
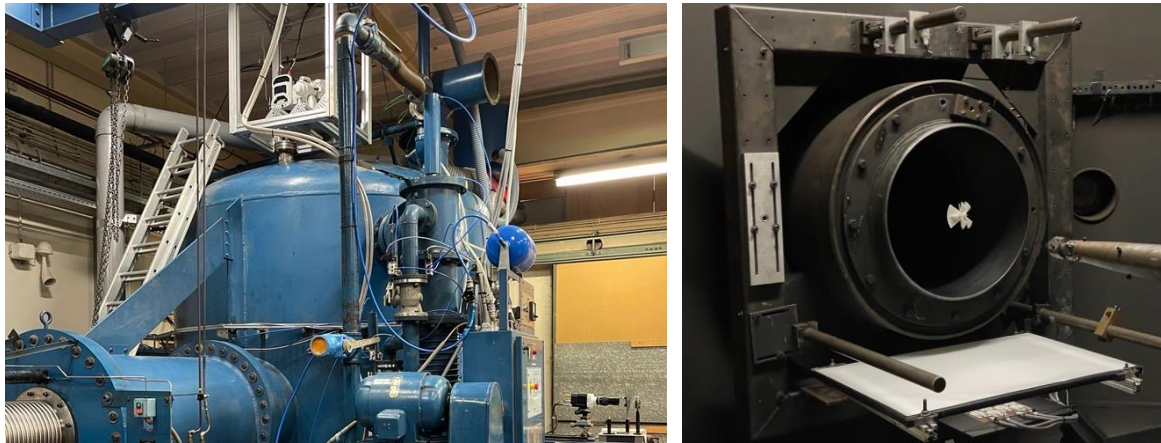

Fig 4. Top and side viewing cameras aligned to observe the test volume.

Compared to the experimental setup introduced in [14], the backlighting apparatus is updated with an improved light source to decrease the motion blur of the images. Four high-power Lumileds Luxeon panels, each equipped with five white LEDs (55 V with 0.7 A per panel), are used to construct a 5x4 array. A comparison between sample images captured using the previous and the new setup in Mach 14 flow is presented in Fig 5. Both images were recorded using the same camera and objective, aperture, and zoom settings. The experiment depicted on the left image (single cube in freestream flow) was recorded with 24.84 µs exposure time, while the test on the right image (cube cluster separation) was captured with 4.98 µs. One can note that the flow luminosity due to the sodium emission, both in the core flow (brightening in the post-shock region) and around the hypersonic jet (overall blur), was less pronounced with the new setup (right image) employing a reduced time. The updated light source provided images of higher contrast that aid in precisely detecting the model boundaries.

A set of reference images is captured to calibrate the visualization system. First, pictures of a checkerboard plate placed at random positions and orientations are snapped by both cameras. Applying a calibration method based on [15] allows the determination of the intrinsic, extrinsic, and distortion properties simultaneously. For the side view, only the distortion properties are reused from this calibration, and images of a scale rule are recorded to determine the scaling factor, i.e., the pixel–to–mm conversion. To link two views and the reference wind coordinate frame, a vertical plumb line is hung, and the calibration board is aligned with the tunnel nozzle. Before the first experiment, a thorough alignment procedure is executed to minimize the orientation correction requirements. The calibration procedure is repeated before each experiment.
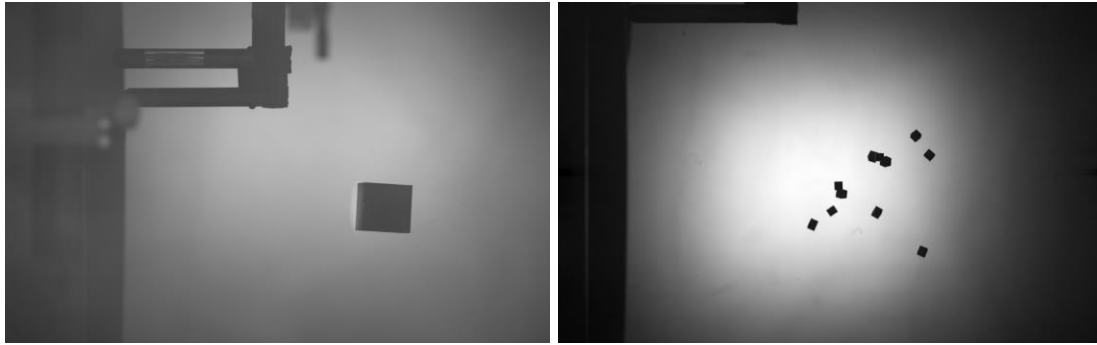
Fig 5. Sample images captured using the previous and the new light sources. Left image: previous setup, 24.84 μs exposure time [14]. Right image: new setup, 4.98 μs exposure time.

2.4. Wind Tunnel Models and Test Matrix

This research aims at comparing the separation dynamics of clusters of different object shapes. Population sizes of 11 and 36 were selected as experimental data exists only for a handful of configurations, and the results obtained for these quantities could be directly compared to the Mach 6 investigations of Whalen and Laurence [11]. The test matrix of the experimental campaign is presented in Table 1 and summarizes five experiments. By increasing the number of test articles, the difficulty of object detection and tracking rises significantly. With a focus on moderate populations, 11 spheres and 11 cubes are examined with a repeat experiment for both, and one test investigates 36 spheres.

Table 1. Test matrix of the experimental campaign summarizing the model and sabot properties.

Test nr.	I.	II.	III.	IV.	V.
Body	Sphere	Sphere	Sphere	Cube	Cube
Population size	11	11	36	11	11
Object size (reference length)	$l_{ref} = D = 6$ mm			$l_{ref} = e = 6$ mm	
Object weight	$m \approx 0.88$ g			$m \approx 1.7$ g	
Sabot internal radius	$r_c = 8.65$ mm		$r_c = 12.4$ mm		

The test articles must be small enough to fit within the core flow region of the hypersonic jet, even in case of larger relative displacements, while providing sufficient visibility in both views. As a consequence, bodies of l_{ref} = 6 mm characteristic length were selected, allowing approximately 20 pixels/edge for the cubes and 50 pixels/circumference for the spheres.

The material of the models was selected based on trajectory predictions computed with the Longshot Free-flight Trajectory Simulator. This tool takes as inputs the model properties (mass and moment of inertia tensor), an aerodynamic database (such as the ones generated by the VKI ANTARES code [16]), transient flow properties (e.g., conditions rebuilt from former Longshot experiments), and starting from arbitrary initial conditions (position, velocity, angle of attack, or body rate) integrates a flight trajectory. The integrator uses equations of motion with six degrees of freedom, provides solutions computed by different methods, such as central differencing and 4th order Runge-Kuta, and can rely on Euler angles or quaternions.

Taking the elementary shape's aerodynamics and the flow conditions expected during the Mach 12 tests, trajectories were computed for different model materials. The calculations showed that steel provides optimal inertia for the chosen model scales, i.e., the objects remain in the core flow region for around 20 ms. Accordingly, stainless steel bearing balls of D = 6 mm and e = 6 mm edge-length cubes are used.

As the goal is to observe the separation dynamics starting from a compact initial configuration, the bodies must be held together by an enclosure that sheds upon the arrival of the flow. The sabot illustrated in Fig 6 and Fig 7 was designed to encapsulate and release the models. The sabot design

started from the concept proposed by Whalen and Laurence [11]. A rib was added to the front flap to improve the structural rigidity, and the flaps were adjusted to increase the lift and the pitching moment at zero angle of attack. The aerodynamics of the half sabot was estimated based on the modified Newtonian theory using the VKI ANTARES code [16]. One must note that this estimation disregards the shock interactions caused by the present non-convex geometry. Following the findings of [12], the hollow hemisphere was filled to remove the cavity for the computation to improve the results. The sabot's parameters, e.g., flap sizes, the material, wall thickness, inertial properties, etc., were iterated by predicting the aerodynamics with the VKI ANTARES code and analyzing shedding trajectory estimates by the Longshot Free-flight Trajectory Simulator (interactions with the fragments, and the other half sabot are neglected). The final sabot geometry's aerodynamic coefficients are computed with a stagnation point pressure coefficient according to Equation 3.19 of [17] (as a function of M = 12 and γ = 1.4) and are presented in Fig 6. The coefficients are normalized by the reference length considered as the external diameter of the hemisphere and by the reference surface computed as a circular area of this diameter.
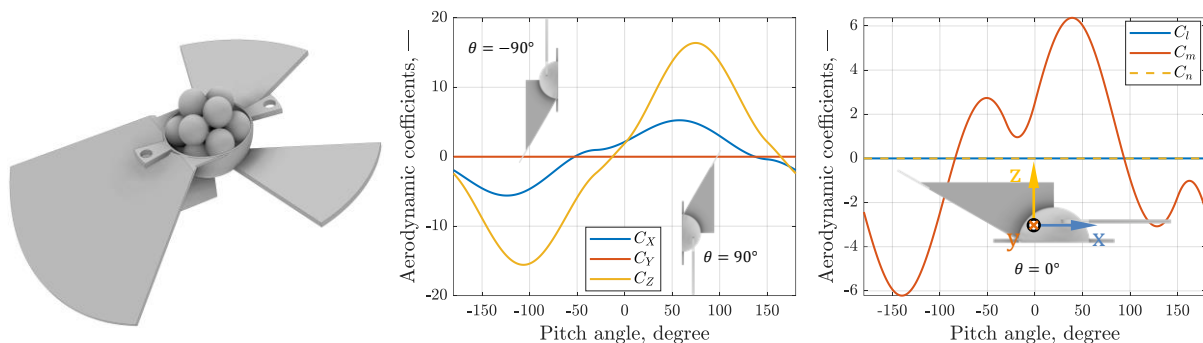

Fig 6. CAD model of the sabot and aerodynamic predictions obtained by the VKI ANTARES code.

The sabots were manufactured in-house with SLA 3D printing from Formlabs Rigid 10K resin. Examples of the printed sabots are presented in Fig 7. The two halves are held together by a 50 μm copper wire loop tied around the tiny alignment flaps. The wires break automatically when the flow arrives. The sabots are positioned in the wind tunnel using suspension wires of the same material. The right-hand-side photo in Fig 4 depicts the sabot assembly suspended in the test section before an experiment.

Fig 7. Pictures of the 3D printed sabot and its assembly.

3. Data Processing Method

3.1. Image processing

The free-flight testing method in the VKI Longshot relies on identifying the model position and attitude based on the silhouette observed throughout the images. The recent development activities focused on accurately determining the position and attitude of a single or a moderate number of objects using the orthogonal camera system. The methodology introduced in [9], [14] is extended during this research to track larger numbers of objects. The image processing procedure is very similar for both views. Since frame locking between the two cameras using unequal sampling frequencies (5 kHz side view and 20 kHz top view) was not possible, the perspectives are processed one after the other, and the transferred data is reused by interpolating in time. First, the side-view images are analyzed. Then,

the determined two-dimensional trajectories are supplied to support the top view processing, where the vertical positions (distances of the objects to the top view camera) are fixed accordingly, and the rest of the trajectory properties are reprocessed. The main steps of the approach are illustrated in Fig 8. The method comprises a blob and edge detection to identify the models on the image (Fig 8a), a blob ID and object ID correlation to determine which silhouette corresponds to which model (Fig 8b), and a precise position and incidence determination step obtained via a contour matching procedure (Fig 8c).
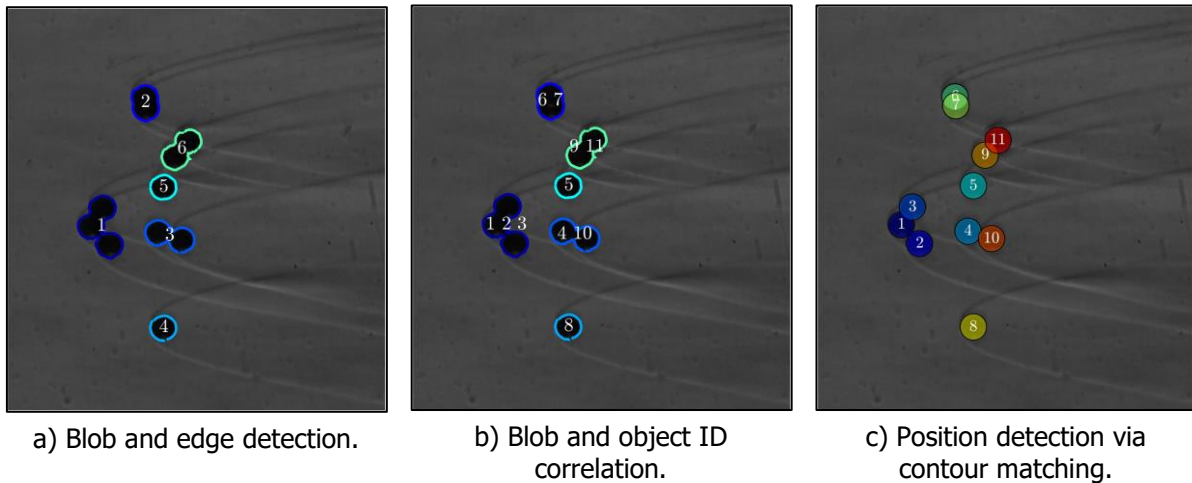
| a) Blob and edge detection. | b) Blob and object ID correlation. | c) Position detection via contour matching. |

Fig 8. Streamline of the image processing.

Blob and edge detection

The blob and edge detection are summarized in Fig 9a–f. The image processing starts by applying a distortion correction to the images based on the earlier calibration. Similarly to the older method [9], [14], an averaged photo is created, and a mask enveloping all the trajectories is defined via user input (Fig 9a). This allows cropping of the original images (Fig 9b) to only the region of interest (Fig 9c). A sub-pixel accurate edge detection is performed within the region of interest of the undistorted image (Fig 9d) to collect all the visible contour points. A binarized photo (Fig 9e) is created to differentiate the objects from the background by applying strong thresholding to the image. The binarized image (Fig 9e) is filtered based on connected pixel island size criteria to remove the noise. Accordingly, several blobs are identified, which correspond to the test objects visible in the image. Each blob encloses one or more objects. Due to the thresholding, these blobs' pixel-level boundaries are rough and located slightly inwards compared to the actual object silhouette (that is visible on the raw image). In the next step, the blobs are analyzed one by one. A barycenter and a silhouette are identified for each blob. The blob silhouette is enlarged by approximately 10–20 %, and the subpixel level edges (detected on the raw image) that fall within this region are selected as the edges of the corresponding blob. Accordingly, the information presented in Fig 9f is obtained, i.e., the blobs visible on the image are detected and numbered with blob IDs, and the corresponding edge points are sorted.

Blob and object ID correlation

After the blob and edge detection are completed for all images, the next task is to correlate the blob IDs between the consecutive images and define which object is enclosed in which blob on each image. The blob IDs are distributed from the image's left to the right side. Hence, the blob numbering may change between images depending on the blobs' displacement between consecutive frames. In practice, if the object enclosed in blob Nr.2 in Fig 9f is faster than the one inside blob Nr.3 on the consecutively recorded image, it would be more downstream, and the blob IDs corresponding to the objects would change. The object ID and blob ID correlation is first attempted with an algorithm that uses the images in reverse order for simplicity since object overlap is less likely to occur at the end of the run. The algorithm assigns an object ID to the blob IDs of the nth image. On the nth-1, new blob/blobs may appear, two or more blobs may merge, one or more blobs may split, or any combination of these. Using the barycenter of the blobs as the positions of the objects identified on the n, n+1, … N, a guess can be provided for their positions on frame n-1. Based on the distance between the guessed object positions and detected blob barycenters and on upwind requirement criteria, the algorithm

distributes the existing and, if required, new object IDs. This process is quite delicate, and due to the complexity of the various possible incidents, it must be proofed manually. When analyzing the top-view images, the blob and object ID association requires another non-automatic validation to ensure agreement with the side-view detection.
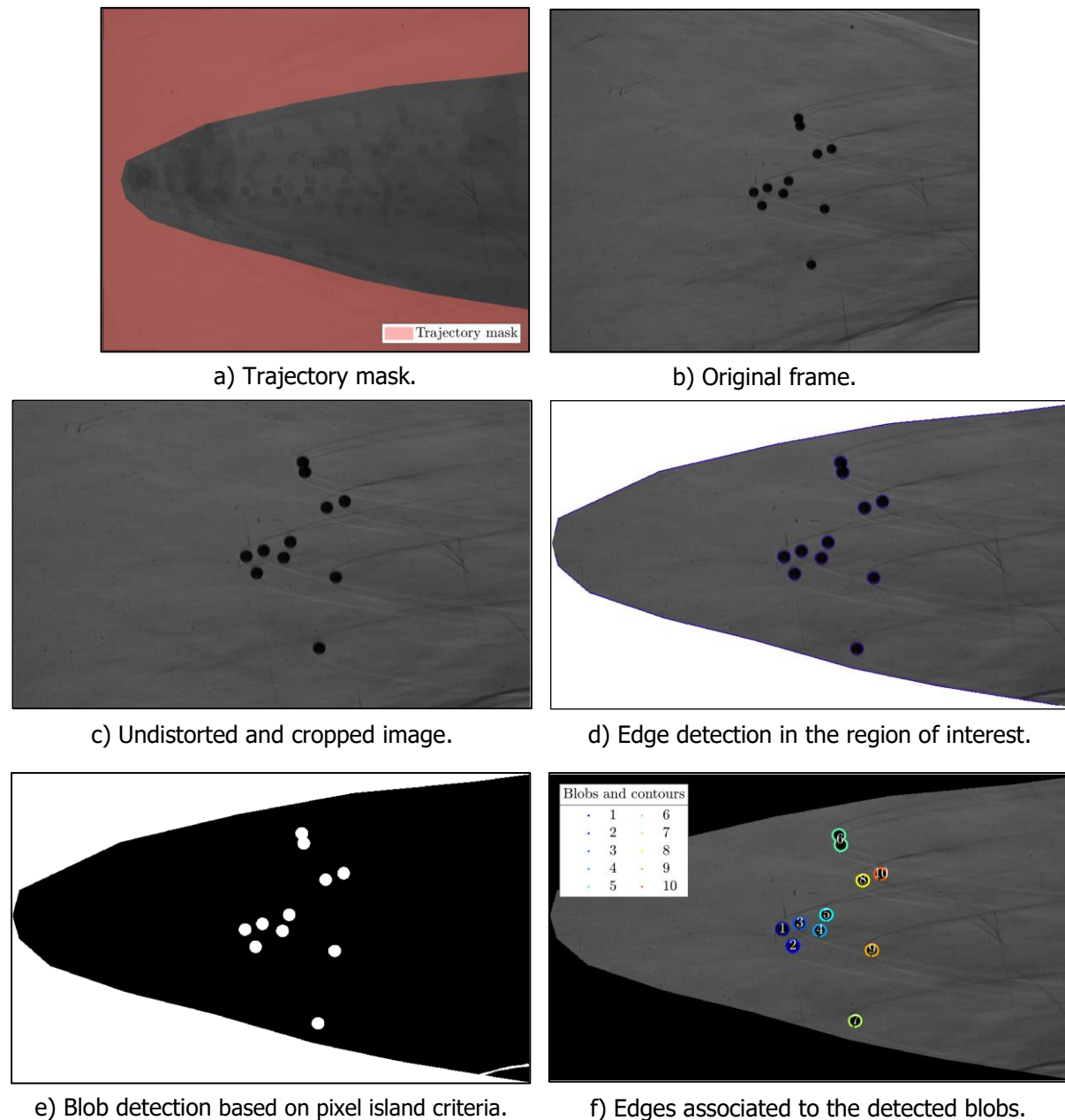

a) Trajectory mask.

b) Original frame.

c) Undistorted and cropped image.

d) Edge detection in the region of interest.

e) Blob detection based on pixel island criteria.

f) Edges associated to the detected blobs.

Fig 9. The blob identification procedure.

Position detection

The objects' position and incidence (in the case of non-spherical bodies) are determined by a contour–matching optimization procedure. Starting from an initial guess on the position and incidence, the test article's CAD geometry is offset, rotated, and projected onto the image plane. Orthographic projections are computed for the side view images, and perspective projections are used for the top view. The algorithm computes the image frame pixel coordinates of the projected silhouette, compares them to the detected edge points, and evaluates a matching error. The optimization is performed with larger bounds on the first image and, in the case of non-spherical objects, with an educated guess on the Euler angles. The guess is supplied automatically for the following images based on the optimization results obtained for the preceding frames. Similarly to the blob and object ID correlation, the position determination is performed in reverse image order, i.e., backward in time. The contour matching is

performed blob-by-blob. Having access to the object's ID that is enclosed in the blob and the associated silhouette coordinates, the contour fitting is performed autonomously. In the case of blobs containing multiple objects, the states of the bodies are optimized together, and the matching error is evaluated using the unified silhouette of the CAD projections. The contour-fitting can proceed without intervention if the blobs merge, split, or regroup since the blob and object IDs are already correlated. Upon the appearance of a new blob that includes multiple objects that were not visible on the formerly processed images, the initial guess needs to be adjusted manually, but after this image, the tracking proceeds automatically. Approaching the initial frames of the recordings, more and more objects are being incorporated in fewer and fewer blobs. As more design variables are present during the optimizations, the computational cost increases significantly. When a large number of objects is packed within a single blob, many will no longer contribute to the formation of the unified boundary. This results in incorrect position and incidence estimates for those objects, which will propagate and perturb the optimization of the earlier image. As in the current research the terminal velocities are of interest, these incorrectly fitted images at the beginning of the trajectory are disregarded.

3.2. Trajectory processing

Even though the measured trajectories are quite smooth, performing numerical differentiation significantly amplifies the noise. This is mitigated by applying 1st-order Savitzky-Golay filters on the trajectory signals. In order to monitor when the free-flight objects exit the core flow region, the transient closure of the hypersonic jet was measured on a few images of the Schlieren side-view recording of the 11-cube experiment. The objects' position is compared to an interpolated local core flow radius during the trajectory analysis. As a body approaches the edge of the zone by 10 mm, the remaining trajectory segment is replaced by a linear extrapolation of the valid flight path. To compare the present results with the ones of [11], the separation velocities are referenced to the cluster's moving center of mass, and time and lateral velocities were normalized using:

$$\tau_s = \sqrt{\frac{\rho_m}{\rho_\infty}} \cdot \frac{R_c}{U_\infty}, \quad t' = \frac{t}{\tau_s}, \quad v_s = \sqrt{\frac{\rho_\infty}{\rho_m}} \cdot U_\infty, \quad V_T' = \frac{V_T}{v_s} \tag{2}$$

where τ_s is the time scale, ρ_m and ρ_∞ are the model and the freestream density, t' is nondimensional time, t is time, R_c is the initial radius of the cluster, U_∞ is the freestream flow speed, v_s is the velocity scale V_T' is the dimensionless lateral velocity, and V_T is the lateral velocity. The flow conditions provided by the Mach 12 contoured nozzle of the VKI Longshot are decaying in time. Applying a time-dependent scaling factor to a velocity signal that rises and converges to a plateau would produce a non-converged dimensionless plot where no terminal velocity could be identified. Therefore, the freestream density and velocity are computed as mean quantities between the moment the sabot first exposes the models to the flow and the instant the objects reach a lateral terminal velocity. To avoid significant test-to-test variations between the scaling factors, the image nr. 1–102 range was used to compute the means (t ≈ 2.5–7.5 ms in Fig 2), translating to t' ≈ 0–1.7 for the small sabot tests and t' ≈ 0–1.2 for the large sabot tests.

4. Results

The dynamic behaviour of the objects is expected to be complex due to the high variability caused by the complex interactions between the objects, such as shock interference, shock impingements, shock wave surfing, collisions, etc. The handful of experiments conducted in this research present results that must be considered observations; they are not sufficient to decide if an 'average outcome' is well represented. Performing a high number of repetitions for each configuration is expected to allow drawing conclusions on a statistical basis.

Fig 10 presents the variation of the normalized lateral velocity of the cluster fragments. The t' = 0 instant corresponds to when the two sabot halves have revealed all the elements of the cluster in the top view, which are still in a compact configuration. The shedding is usually completed within 0.5 ms after the reveal, i.e., approximately at t' ≈ 0.15. It must be noted that the sabot opening must have an influence on the initial part of the separation due to shockwave impingements; however, the discard is usually fast, around 1.7-2.5 ms starting from the arrival of the flow to the test section (out of which flow establishment takes around 1.6 ms). The plots indicate the vertical and spanwise spread normalized by the reference length of the objects at t' = 5. The colored lines represent individual objects.
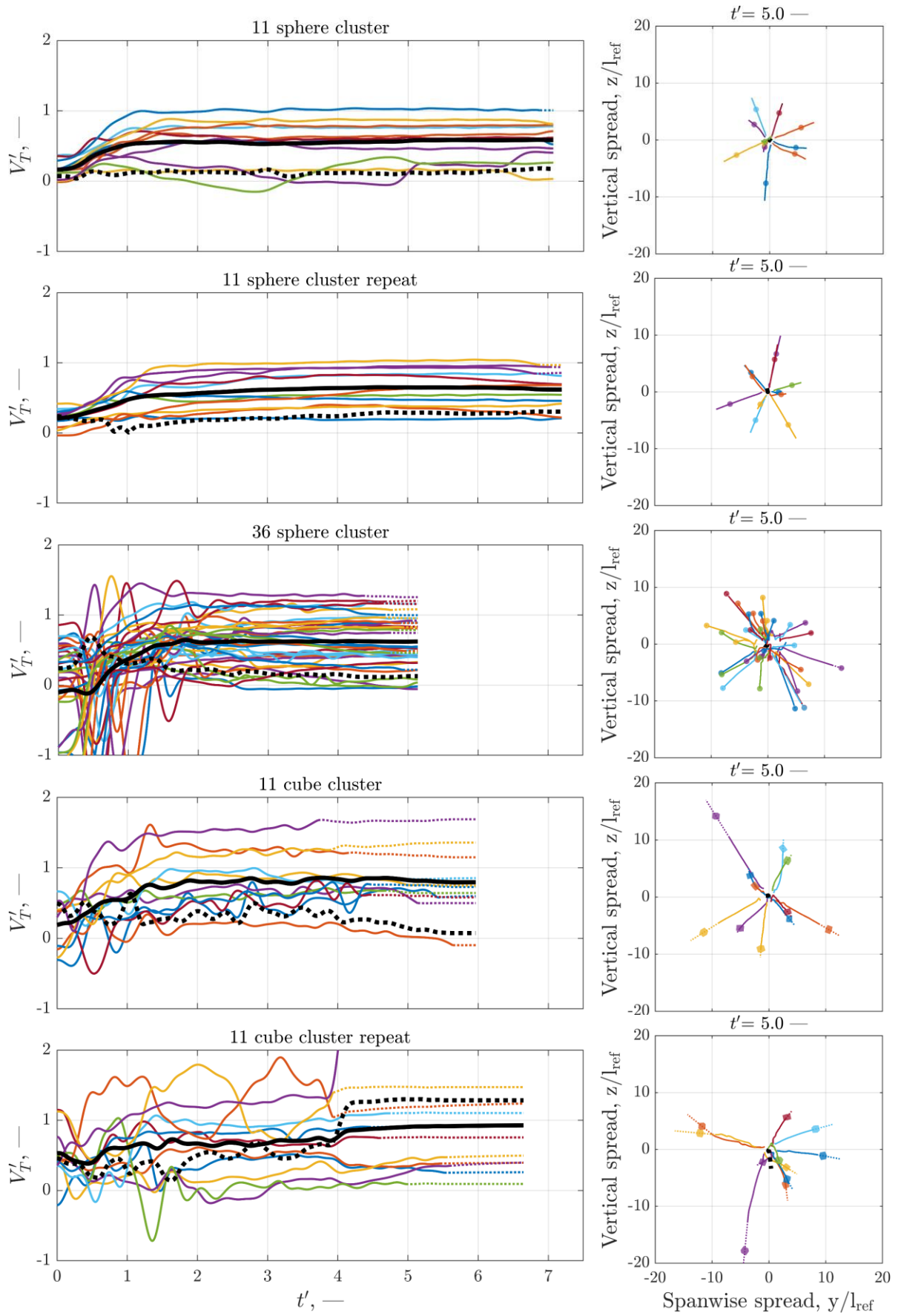
Fig 10. Dimensionless separation velocities and normalized spreading.

The solid parts of the curves show the flight inside the core flow region, and the dotted counterparts are derived from the linear extrapolations of the trajectory as the objects approach or exit the core flow. The solid black lines indicate the mean of the lateral velocity, and the dotted black lines show the velocity of the center of mass. The transversal separation velocities seem to reach a terminal value by $t' = 2$, except for the 11 cube repeat test, where one object exhibits attitudes causing a strong negative lifting later on. The separation velocities of the 11 sphere tests are smoother than those of the other tests, probably due to the non-lifting characteristics of the spheres. Observing the normalized terminal velocity (V_T') plot of the 11-sphere test in Fig 10, one can note bumps in the three curves (purple, green, and yellow) passing close to zero. This is due to the fact that the objects plotted by purple and green were traveling inside the shocked region of the body denoted by yellow, collided with each other, and later on, collided with the leading body. The large fluctuations observed at the initial part of the 36 object curves are caused by the failure of the tracking as the populated cluster is tightly packed. During the 11-cube repeat test, two bodies (denoted by orange and yellow) stuck together and spun throughout time history.

Fig 11 compares the dispersion of the clusters in terms of separation velocities and the radial (R_S) and axial spreads (A_S). The plots on the left show the mean curves with error bars spanning the minimum and maximum values measured at specific instances, with a Rayleigh distribution fit representing the occurrence of the instantaneous values. The 11-sphere tests show quite good repeatability. The spread and velocity distribution of the spheres are more confined than those of the cube experiments. Increasing the number of spheres seems to increase the radial spreading and the spread of the terminal velocity. The plots on the right compare the radial and axial spread, i.e., the mean distance of the fragments from the cluster's center of gravity normalized by the characteristic length. As also reported by Whalen and Laurence in [11] for one of their sphere experiments, the fragments undergo a slight initial axial compression and a sharp radial expansion up to approximately $t' = 2$. The cubes produce a greater spread than the spheres; however, they seem to undergo milder flattening.
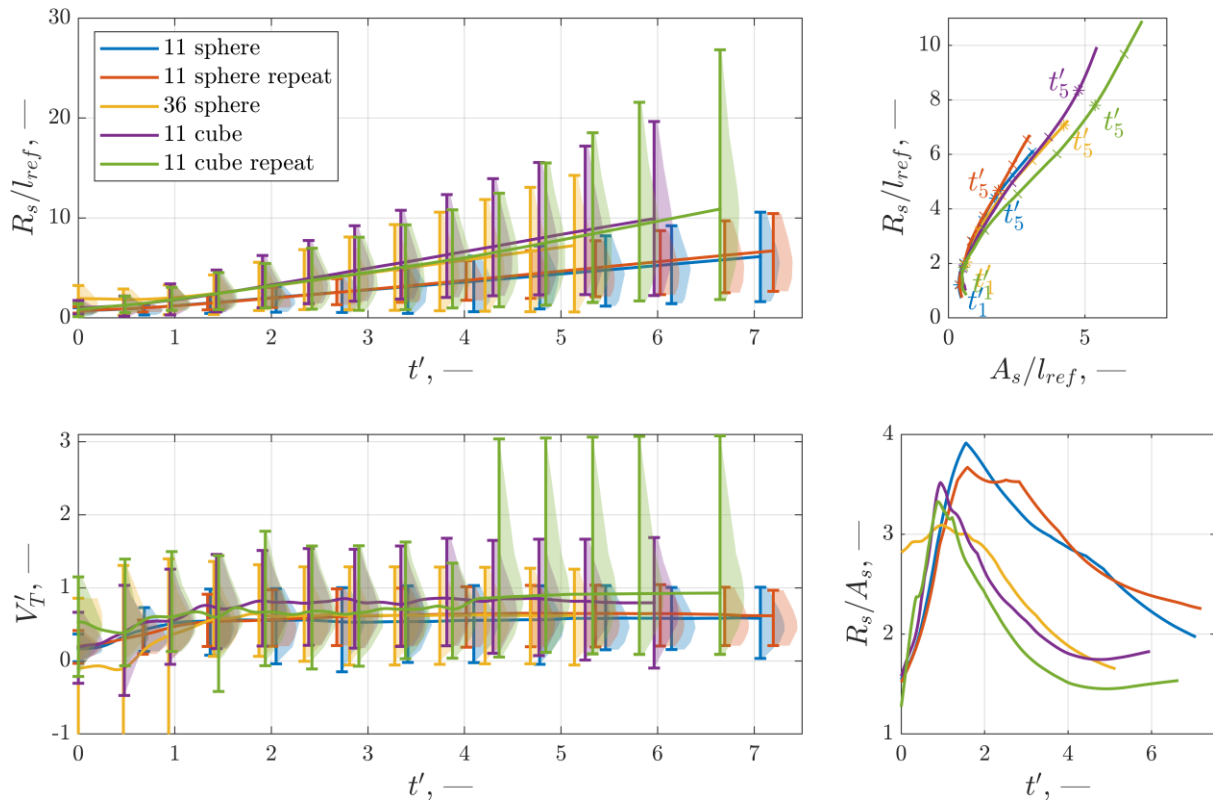

Fig 11. Comparison of nondimensional radial separations and separation velocities. Rayleigh distributions are fitted on the individual values at specific time instants.

The mean and maximum lateral terminal velocities extracted at $t' = 5$ are compared to the results of [10] and [11] in Fig 12. The mean values of the 11 sphere tests ($V_T' = 0.57$, $V_T' = 0.65$) demonstrate a fair agreement with the correlation proposed by Park and Park ($V_T' = 0.51$) and the results of Whalen and Laurence ($V_T' = 0.54$); meanwhile, the 36 sphere experiment yielded a lower mean ($V_T' = 0.62$)

and maximum velocity indicating a more significant discrepancy compared to the Mach 6 measurement (V'_T = 0.80) and the correlation (V'_T = 0.93). Even though the more populated cluster's mean lateral terminal velocity is approximately the same as the one found in the case of the 11 sphere tests, the spread of the terminal velocities is wider. The 11 cube tests yielded considerably higher terminal velocities (V'_T = 0.83, V'_T = 0.91) and substantial maximal speeds than the sphere experiments.
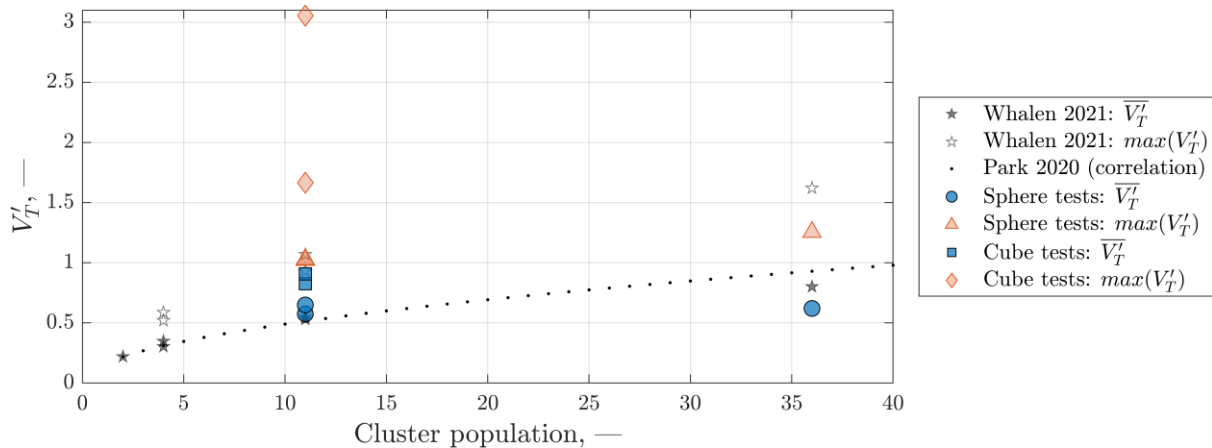

Fig 12. Comparison of the lateral terminal velocities.

5. Conclusion

This paper presents an experimental campaign studying the separation of clusters in Mach 12 cold hypersonic flow. The tests were executed in the VKI Longshot wind tunnel employing a dual-camera free-flight measurement technique. Updates to the backlighting setup improved the visualization quality by permitting the reduction of the exposure time for reduced motion blur. The models are initially kept in place and released upon the flow's arrival by an expendable sabot consisting of two halves. The system performed well; however, the automatic discard of ~2 ms could be accelerated further by decreasing the weight of the sabot. The sabot encloses the models during the flow start-up, which is advantageous. Still, as the sabots shed, interactions between them and the fragments may perturb the initial part of the separation dynamics, which is not straightforward to quantify. The image processing routines have been upgraded to identify multiple blobs and their associated boundaries. A new algorithm was implemented to correlate the blob and object IDs throughout the images; however, this process is challenging due to the complexity of the various possible incidents and must be manually revised. Such manual revisions are very time-consuming, given that the identification method must be reworked in the future, e.g., by performing the detection, identification, and contour matching steps together so they can inform each other. The object ID association between the two views must also be automated since it is cumbersome to do manually and prone to human error.

In addition to the tests of 11 and 36 spheres, which Whalen and Laurence [11] investigated earlier at a lower Mach number of 6, 11 cubes were tested for the first time. The current 11 sphere experiments demonstrated a fair agreement with the data of [11] and the correlation of [10], while the 36 sphere test yielded lower terminal velocities. Clusters of objects capable of generating lift showed greater dispersal. The significant difference between the sphere and cube cluster observations in terms of mean values and distributions confirms that the object shape can significantly affect the separation. The mean value and the distribution of the terminal velocities indicate a reasonable consistency for the repeated experiments; however, such fragment separation is expected to be complex. Therefore, a high number of repetitions must be performed for each configuration to draw clear conclusions on a statistical basis. Additionally, since the downstream parts of the trajectories are of interest, future experiments could focus on the later trajectory segments by mounting the sabot upstream into the nozzle or employing smaller models.

References

[1] Q. R. Passey and H. J. Melosh, "Effects of Atmospheric Breakup on Crater Field Formation," *Icarus*, vol. 42, pp. 211–233, 1980.

[2] N. A. Artem'eva and V. V. Shuvalov, "Interaction of shock waves during the passage of a disrupted meteoroid through the atmosphere," *Shock Waves*, vol. 5, pp. 359–367, 1996.

[3] S. J. Laurence, R. Deitering, and H. G. Hornung, "Proximal bodies in hypersonic flow," *J Fluid Mech*, vol. 590, pp. 209–237, 2007, doi: 10.1017/S0022112007007987.

[4] S. J. Laurence, N. J. Parziale, and R. Deiterding, "Dynamical separation of spherical bodies in supersonic flow," *J Fluid Mech*, vol. 713, 2012, doi: 10.1017/jfm.2012.453.

[5] S. J. Laurence and R. Deiterding, "Shock-wave surfing," *J Fluid Mech*, vol. 676, pp. 396–431, 2011, doi: 10.1017/jfm.2011.57.

[6] P. J. Register *et al.*, "Interactions between asteroid fragments during atmospheric entry," *Icarus*, vol. 337, p. 113468, 2020, doi: https://doi.org/10.1016/j.icarus.2019.113468.

[7] S. H. Park, J. Kim, I. Choi, and G. Park, "Experimental study of separation behavior of two bodies in hypersonic flow," *Acta Astronaut*, vol. 181, no. June 2020, pp. 414–426, 2021, doi: 10.1016/j.actaastro.2021.01.037.

[8] D. G. Kovács, G. Grossir, G. Dimitriadis, and O. Chazot, "Space debris interaction across a two-dimensional oblique shock wave," *Exp Fluids*, vol. 64, no. 8, pp. 1–17, 2023, doi: 10.1007/s00348-023-03686-9.

[9] D. G. Kovács, G. Grossir, G. Dimitriadis, and O. Chazot, "Free-flight testing of proximal spheres and cubes in Mach 14 hypersonic flow," in *10th European Conference for Aeronautics and Space Sciences (EUCASS)*, Lausanne, Switzerland, 2023, pp. 1–10.

[10] S.-H. Park and G. Park, "Separation process of multi-spheres in hypersonic flow," *Advances in Space Research*, vol. 65, no. 1, pp. 392–406, 2020, doi: 10.1016/j.asr.2019.10.009.

[11] T. J. Whalen and S. J. Laurence, "Experiments on the separation of sphere clusters in hypersonic flow," *Exp Fluids*, vol. 62, no. 4, 2021, doi: 10.1007/s00348-021-03157-z.

[12] G. Grossir *et al.*, "Aerodynamic characterization of space debris in the VKI Longshot hypersonic tunnel using a free-flight measurement technique," *Exp Fluids*, vol. 61, no. 7, 2020, doi: 10.1007/s00348-020-02995-7.

[13] G. Grossir, S. Paris, K. Bensassi, and P. Rambaud, "Experimental Characterization of Hypersonic Nozzle Boundary Layers and Free-Stream Noise Levels," 2013.

[14] D. G. Kovács, G. Grossir, G. Dimitriadis, and O. Chazot, "Six Degrees of Freedom Free-flight Measurement in the VKI Longshot Wind Tunnel," in *AIAA AVIATION 2023 Forum*, American Institute of Aeronautics and Astronautics, Inc., 2023, pp. 1–16. doi: 10.2514/6.2023-3535.

[15] Z. Zhang, "A Flexible New Technique for Camera Calibration," Redmond, USA, 1998.

[16] T. Durbin, G. Grossir, and O. Chazot, "Hypersonic aerodynamic predictions for arbitrary geometries using ANTARES," in *2nd International Conference on High-Speed Vehicle Science & Technology*, Brugge, 2022.

[17] J. D. Anderson, *Hypersonic and high temperature gas dynamics*, 2nd ed. Reston, Virginia, United States of America: American Institute of Aeronautics and Astronautics, 2000. doi: 10.1007/s13398-014-0173-7.2.